CHEMISTRY
A EUROPEAN JOURNAL

DOI: 10.1002/chem.200701970

Self-Assembled 3D Architectures of $LuBO_3:Eu^{3+}$: Phase-Selective Synthesis, Growth Mechanism, and Tunable Luminescent Properties

Jun Yang, Chunxia Li, Xiaoming Zhang, Zewei Quan, Cuimiao Zhang, Huaiyong Li, and Jun Lin*[a]

Abstract: Rhombohedral-calcite and hexagonal-vaterite types of $LuBO_3:Eu^{3+}$ microparticles with various complex self-assembled 3D architectures have been prepared selectively by an efficient surfactant- and template-free hydrothermal process for the first time. X-ray diffraction, scanning electron microscopy, energy-dispersive X-ray spectrometry, transmission electron microscopy, high-resolution transmission electron microscopy, selected area electron diffraction, photoluminescence, and cathodoluminescence spectra as well as kinetic decays were used to characterize the samples. The pH, temperature, concentration, solvent, and reaction time have a crucial influence on the phase formation, shape evolution, and microstructure. The reaction mechanism is considered as a dissolution/precipitation process; it is proposed that the self-assembly evolution occurs by homocentric layer-by-layer growth. Under UV excitation and low-voltage electron beam excitation, calcite-type $LuBO_3:Eu^{3+}$ particles show a strong orange emission corresponding to the $^5D_0 \rightarrow ^7F_1$ transition of Eu^{3+} whereas vaterite-type $LuBO_3:Eu^{3+}$ particles exhibit a strong red emission with much higher R/O values (that is, chromatically redder fluorescence than that of crystals grown from a direct solid-state reaction). The tunable luminescent properties have potential applications in fluorescent lamps and field emission displays.

Keywords: europium · hydrothermal synthesis · luminescence · lutetium orthoborates · self-assembly

Introduction

Generally, the chemical and physical properties of inorganic micro-/nanostructures are related fundamentally to their chemical composition, size, phase, surface chemistry, shape, and dimensionality.[1] Therefore rational control over these factors has become an important research issue in recent years,[2] allowing us not only to observe unique properties of the materials, but also to tune their chemical and physical properties as desired. Nanomaterials have many interesting properties that differ from those of the bulk materials.[3] However, most nanomaterials often have a natural tendency toward aggregation, which is always assumed to be the main hindrance to their practical application. Rare earth orthoborates that are apt to form highly agglomerated particles are a representative example.[4] Therefore, it is challenging and important to synthesize materials with a specific hierarchical and complex 3D structure, composed of nanocrystals (nanoparticles, nanorods, nanoribbons, nanosheets, and so forth) arranged in a particular way. It is very useful for practical applications that such materials not only possess some improved properties originating from their building blocks, namely nanocrystals, but also at the same time solve the problem of nanomaterial agglomeration. The simplest synthetic route to 3D nanostructures is probably self-assembly, in which ordered aggregates are formed in a spontaneous process.[5] The self-assembly of anisotropic nanostructures, such as nanoplates, nanosheets, nanorods, and nanotubes, requires more effort than the isotropic self-assembly of spherical or near-spherical nanoparticles. In the controlled self-assembly of 1D or 2D nanobuilding blocks into novel 3D nanoarchitectures, copolymers and surfactants always play important roles[6] owing to their directing functions during

---

[a] J. Yang, C. Li, X. Zhang, Z. Quan, C. Zhang, H. Li, Prof. J. Lin
State Key Laboratory of Rare Earth Resource Utilization
Changchun Institute of Applied Chemistry
Chinese Academy of Sciences, Changchun 130022 (P.R. China)
and
Graduate University of the Chinese Academy of Sciences
Beijing 100049 (P.R. China)
Fax: (+86) 431-8569-8041
E-mail: jlin@ciac.jl.cn

Supporting information for this article is available on the WWW under http://www.chemeurj.org/ or from the author.

the aggregation process as well as their stabilizing effects in equilibrium systems. However, the process is complicated, and the resulting structures are not stable enough for practical applications. From a technical viewpoint, a simple, clean, and controllable approach to durable self-assembled 3D architectures, is desired, not only because of the importance of understanding the concept of self-assembly with artificial building blocks, but also the great potential for applications. However, knowledge about surfactant- and template-free self-assembly of nanomaterials into complex 3D hierarchical nanostructures is still very limited.[7]

Orthoborate-based phosphors have attracted much attention owing to their high stability, low synthetic temperature, and high UV and optical damage threshold.[8] Rare earth orthoborates $LnBO_3$ (Ln = lanthanides, yttrium) have proven very useful host lattices for the luminescence of Eu^{3+} and Tb^{3+}, which have found wide application in Hg-free fluorescent lamps and various kinds of display devices.[9] A problem in the application of these materials is their relatively poor color purity. Eu^{3+}-doped $LnBO_3$, for example, has an emission spectrum composed of the stronger $^5D_0 \rightarrow ^7F_1$ and weaker $^5D_0 \rightarrow ^7F_2$ transitions, which give rise to an orange-red color instead of deep red and thus hamper its application. The latter transitions are hypersensitive to the symmetry of the local crystal fields surrounding the Eu^{3+} ions, and relatively strong when the symmetry of the crystal field is relatively low. Preparation of nanosheets with a large surface area (more Eu^{3+} with low crystal field symmetry near the surface) is an effective method of lowering the symmetry of the Eu^{3+} local environment in the YBO_3 host and of improving the R/O value.[4a,10] Therefore, improvement of the performance, as well as any sensible interpretation of the luminescent properties, requires these compounds to have a well-defined crystal structure.[8a]

Lutetium orthoborates ($LuBO_3$), owing to their high density and high damage thresholds, have been considered as promising host matrices for substitution of lanthanide ions to produce phosphors, lasers, or scintillators.[11] They crystallize in two polymorphs, that is, a rhombohedral-calcite phase and a hexagonal-vaterite phase with different crystal field symmetry,[12] which can result in different luminescent properties of the doped Eu^{3+} ions. As a result, the selective synthesis of calcite and vaterite types of $LuBO_3$ not only has great theoretical significance in the study of the polymorph conversion/phase transition processes and the phase-dependent properties, but is also very important for their potential applications. $LuBO_3$:Eu^{3+} phosphors derived from the conventional solid-state reaction and sol-gel process have bad irregular shapes and agglomerated particles with lower R/O values[13] due to the high annealing temperature and repeated grinding process, which limits their dispersing stability and subsequent coating ability on the display panels with chromatically redder fluorescence.[9d] Accordingly, $LuBO_3$:Eu^{3+} phosphors with homogeneous, monodispersed, and well-defined morphology are highly desired. It is well known that the hydrothermal method is a promising synthetic route, which can be better controlled through judicious choice of molecular precursor and reaction parameters, such as time and temperature, to give highly pure and homogeneous materials. The technique allows a low reaction temperature and controllable size, phase, and morphology of the products.[14] All reports on the hydrothermal/solvothermal synthesis and properties of rare earth orthoborate materials have been focused on YBO_3, $GdBO_3$, and $NdBO_3$.[4a,10,15] To the best of our knowledge, no studies of the hydrothermal/solvothermal synthesis of $LuBO_3$ have been reported.

Herein, we report an efficient surfactant- and template-free hydrothermal approach to synthesize rhombohedral and hexagonal $LuBO_3$:Eu^{3+} selectively with novel self-assembled 3D architectures. These microparticles composed of nanosized units were expected to maintain the desirable properties of $LuBO_3$:Eu^{3+} nanocrystals (flakes) while being quite stable on the micrometer scale. The influences of pH, temperature, concentration, solvent, and reaction time on the phase formation and shapes have been investigated in more detail than in the previous work on $LnBO_3$.[4a,10,15] The luminescent properties of the different phases and shapes of $LuBO_3$:Eu^{3+} have also been compared with the products obtained directly from conventional solid-state reaction. Improved chromaticity (chromatically redder fluorescence) can be obtained in these flower-like nanoflake assemblies. This improvement was especially important for a red phosphor such as vaterite-type $LuBO_3$:Eu^{3+}, whose application had always been restricted by its relatively poor chromaticity.

Results and Discussion

Phase-selective synthesis: The pH has a significant influence on the particular phase formation of crystallized lutetium orthoborates. X-ray diffraction (XRD) patterns for samples obtained at different pH values have shown that lutetium orthoborates crystallize into two different phases (Figure 1). At pH 4 (sample 1), all diffraction peaks can be readily indexed to the pure rhombohedral-calcite phase of $LuBO_3$ with the cell parameters $a = 4.9153$ Å, $c = 16.212$ Å (JCPDS: 72-1053) (Figure 1a). When the pH is increased to 7–8 (samples 3 and 4), all the diffraction peaks can also be indexed as a pure hexagonal-vaterite phase of $LuBO_3$ with cell parameters $a = 3.727$ Å, $c = 8.722$ Å (JCPDS: 74-1938) (Figure 1b,c). No additional peaks of other phases have been found, indicating that Eu^{3+} has been effectively built into the $LuBO_3$ host lattice. The relative intensity ratios of the diffraction peaks (104) at pH 4 and (002) at pH 8 are much higher than the conventional value, indicating that the samples tend to be oriented preferentially. Moreover, high crystallinity can be obtained at a relatively low temperature. This is important for phosphors, since high crystallinity always means fewer traps and stronger luminescence. If the solution pH is adjusted to 5.5 (sample 2), the hydrothermally obtained product is a mixture of the rhombohedral-calcite and hexagonal-vaterite phases of $LuBO_3$:Eu^{3+} (see Figure S1 in the Supporting Information). The difference in our

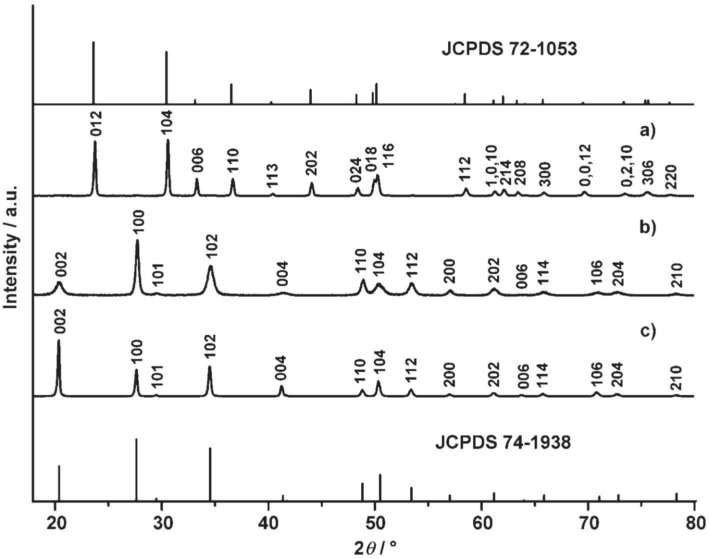

Figure 1. XRD patterns of the samples obtained at different pH values: a) sample 1, pH 4; b) sample 3, pH 7; c) sample 4, pH 8. The standard data for calcite-type $LuBO_3$ and vaterite-type $LuBO_3$ (JCPDS card 72-1053 and 74-1938, respectively) are also presented for comparison.

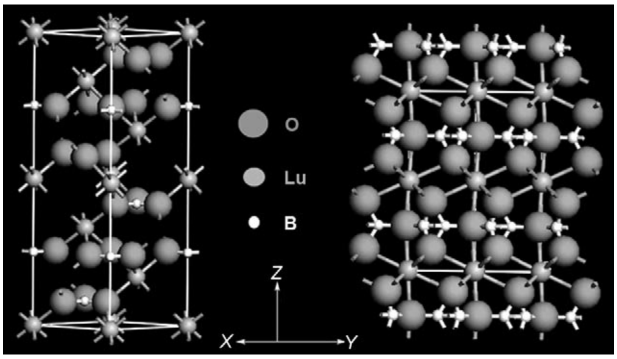

Figure 2. Simulated crystal structures of calcite-type $LuBO_3$ (left) and vaterite-type $LuBO_3$ (right).

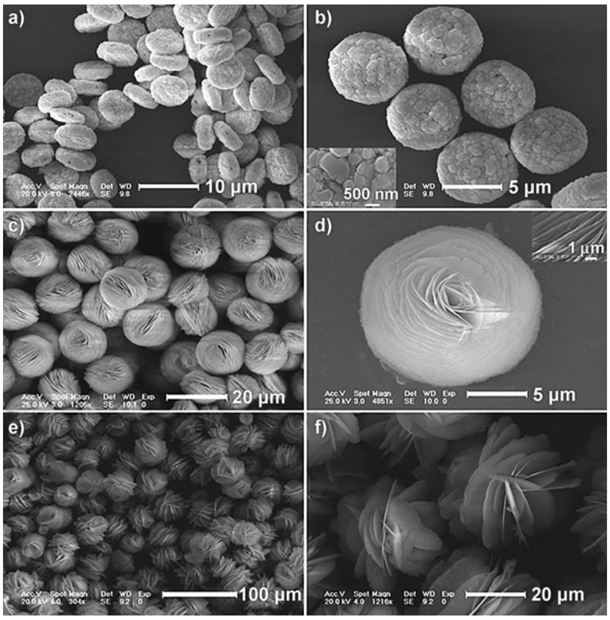

Figure 3. SEM images of the samples obtained at different pH values: a,b) sample 1, pH 4; c,d) sample 3, pH 7; e,f) sample 4, pH 8.

present work from that reported previously is that the slightly smaller Lu^{3+} ion replaces $Y^{3+}/Gd^{3+}/Nd^{3+}$ in the isostructural host lattice.[4a,10,15] This allows the preparation of both the calcite and vaterite phases by a low-temperature hydrothermal method. Here, $LuBO_3$ crystallizes in two polymorphs with differing symmetry of the crystal field, which can result in different luminescent properties of the doped Eu^{3+} ions. This case is quite different from that of Y/Gd/$NdBO_3$.

Calcite-type $LuBO_3$ exhibits a rhombohedral structure with space group $R\bar{3}c$ (D^{6}_{3d}). The lutetium ion occupies a single S_6 symmetry site with a six-fold coordination to oxygen atoms.[16] Vaterite-type $LuBO_3$ crystallizes in the $P6_3/mmc$ (C^{2}_{h}) space group. The coordinative polyhedron consists of eight oxygen atoms in the form of a capped trigonal antiprism with two axial ligands. Two types of environment for the rare earth cation are reported with lower symmetry than S_6 because of the delocalization of oxygen atoms leading to a deviation from the ideal S_6 local symmetry.[12] The crystal structures of these two different phases are shown in Figure 2.

Morphology: The pH also has a significant effect on the morphology and microstructures of $LuBO_3$:Eu^{3+}. The scanning electron microscopy (SEM) image of the sample obtained at pH 4 (sample 1; Figure 3a,b) exhibits wheel-like shapes with rough surfaces. As seen in Figure 3b, the products are complete wheels with a narrow size distribution, a diameter of around 5.7–6.4 μm and a height of about 2 μm. Detailed surface observation (Figure 3b, inset) implied that each microwheel was constructed from smaller nanoparticles. Hydrothermal treatment of an initial solution with pH 7 (sample 3), resulted in the formation of vaterite-type $LuBO_3$:Eu^{3+} flower-like microstructures, diameter about 15 μm (Figure 3c,d), each constructed from densely curved nanoflakes around 40 nm thick (Figure 3d, inset). When the pH of the initial solution was adjusted to 8 with aqueous ammonia solution (sample 4), another vaterite type of $LuBO_3$:Eu^{3+} microflowers was obtained (Figure 3e) which were nearly monodisperse, with average diameter around 30–43 μm. Figure 3f reveals that a single flower-like microstructure is composed of many petal-like nanoflakes with a uniform thickness of about 45 nm and smooth surfaces. The microarchitectures are loose and highly porous, and most of the nanoflakes are linked together by both edge-to-edge and edge-to-surface conjunctions; the nanoflakes extend outward from the center of the microstructure, and a few are attached to each other. Therefore, such an architecture is a result of self-assembly.[6b] Energy-dispersive X-ray (EDX) spectroscopy To characterize the composition of the as-prepared product further, the EDX spectrum (see Figure S2 in the Supporting Information) of sample 4 shows the presence of Lu, O, B, and Eu, in agreement with $LuBO_3$ and Eu^{3+} being effectively built into the $LuBO_3$ host lattice. If the solution pH is adjusted to 5.5 (sample 2), the hydrothermally obtained product is a mixture of wheel-like shapes and flowers (see Figure S3 in the Supporting Information).

The fine structure of the flowers described above were studied by transmission electron microscopy (TEM). A broken flake of the flower (sample 4; Figure 4a), obtained by ultrasonic treatment for about 30 min, has a sector-like morphology, which comes from the petal-like nanoflake (Figure 3f), and measures about 10 μm along the radial axis. The corresponding selected area electron diffraction (SAED) pattern of the broken nanoflake taken along the [001] zone axis (Figure 4b) reveals that the nanoflake ED pattern is characteristic of a hexagonal $LuBO_3$:Eu^{3+}, in accordance with the XRD result. Moreover, SAED patterns taken both from different areas on a single fragment and from different fragments were identical within experimental accuracy, indicating that the $LuBO_3$:Eu^{3+} nanoflakes are single-crystalline and that different nanoflakes have identical crystallization habits. The patterns also reveal that the nanoflakes are stable enough to withstand the irradiation of convergent high-energy electron beams. Figure 4c is a high-resolution TEM image of the same $LuBO_3$:Eu^{3+} nanoflakes as in Figure 4a, taken with the electron beam along the [001] zone axis, perpendicular to the wide surface of the flake. The lattice fringes show the imaging characteristics of the hexagonal $LuBO_3$ crystal, in which the *d* spacing of 0.32 nm corresponds to the distance between the (100) planes. Further analysis indicates that the $LuBO_3$:Eu^{3+} nanoflake grows along the [100] or [010] crystallographic direction and is enclosed by ±(001) facets,[17] that is, the widest facets, as suggested by the XRD measurement.

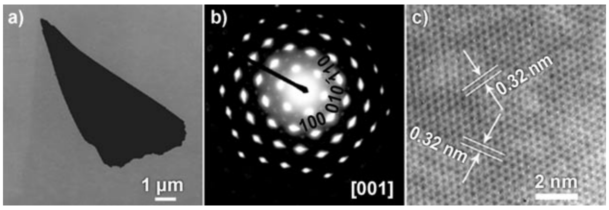

Figure 4. a) Representative TEM image of the $LuBO_3$:Eu^{3+} nanoflake shed from the microflower (sample 4) after ultrasonic treatment for 30 min; b) the corresponding electron diffraction pattern; c) HRTEM image of the broken nanoflake shown in a).

Generally, the growth process of crystals can be classified in two steps: an initial nucleating stage and a crystal growth stage.[18] At the initial nucleation stage, the formation of the seeds is crucial for further growth of the crystals. The subsequent crystal growth stage is a kinetically and thermodynamically controlled process that can form different shapes with some degree of shape tenability through changes in the reaction parameters such as temperature, reaction time, concentration, solvent, and pH.[14f,19] In the present system, the pH of the solution is undoubtedly vital in the formation of these 3D architectures, as shown in Figure 3.

Temperature has been found to play an important role in the crystallization and shape control of $LuBO_3$:Eu^{3+}. At pH 8 and reaction temperature 120 °C, no product could be obtained. Flower-like aggregates composed of porous nanopetals (sample 5) were obtained at 160 °C which were similar to those obtained at 200 °C (Figures 5a,b and 3e,f), but smaller. When the hydrothermal temperature was increased to 240 °C (sample 6), imperfect flowers assembled from nanoflakes were observed with dimensions below 18 μm, along with many single nanoflakes (Figure 5c,d_1,d_2,). It is very interesting that these nanoflakes are in the shape of normal sectors (Figure 5d_2). With the solution at a constant initial pH (pH 8), a decreasing concentration of H_3BO_3 (50 % excess, sample 7) results in a huge variety of product shapes (Figure 6). All the products are in the form of microspheres, diameter about 10 μm, each constructed from densely packed nanoflakes about 25 nm thick (Figure 6b, inset). Different solvents were tested to check their effects on the syntheses.[10,20] The results indicated that the use of diethylene glycol (DEG) results in the formation of only a highly monodisperse distribution of doughnut-shaped particles with a mean size of 11 μm at pH 8 (sample 8, Figure 7), which comprise nanoflakes arranged at progressively increasing angles to the radial axis from two sides. In addition,

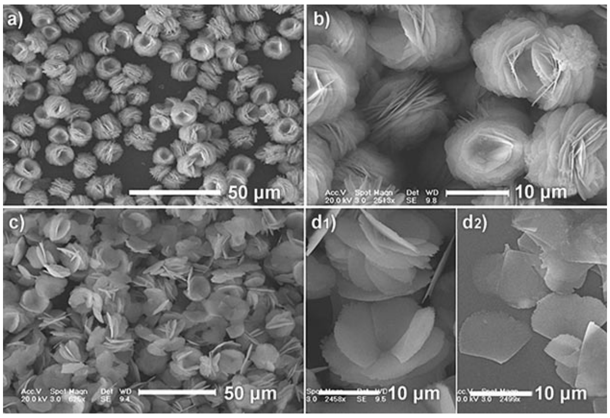

Figure 5. SEM images of the samples obtained at different hydrothermal temperatures: a,b) sample 5, $T=160\,°C$; c,d_1,d_2) sample 6, $T=240\,°C$.

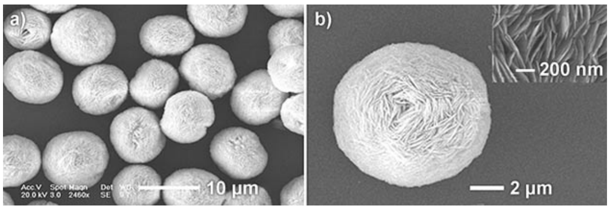

Figure 6. SEM images of the samples obtained at a 50 % of excess H_3BO_3 (sample 7).

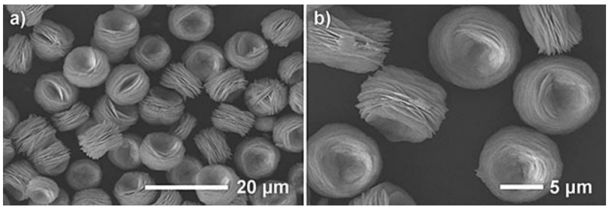

Figure 7. SEM images of the samples obtained using a mixture of H_2O and DEG as solvent (sample 8).

these microdoughnuts are much smaller than microflowers under the same conditions except for the use of DEG.

We investigated the influence of postcalcination temperature on the morphology and crystallinity of the products obtained. The SEM images of sample 4 after calcination at 1000 °C for 4 h (Figure 8) show that through calcination the assembled particle size and external shape remain the same as those of the uncalcined samples (Figure 3e,f). More importantly, the characteristic morphology of the nanoflakes is unchanged (Figure 8b) owing to the higher activation energies needed for the collapse of these structures (good thermal stability),[14e,f] although the relatively high surface energy may cause partial melting of the edges of the nanoflakes, and the surface tension results in the net-like structure on the edges, which differs from that previously reported for lanthanide orthoborates[4a] and much better than the badly irregularly shaped and agglomerated sample obtained by a direct solid-state reaction (see Figure S4 in the Supporting Information). In addition, the crystallinity, as expected, can be greatly improved through postcalcination.[4a]

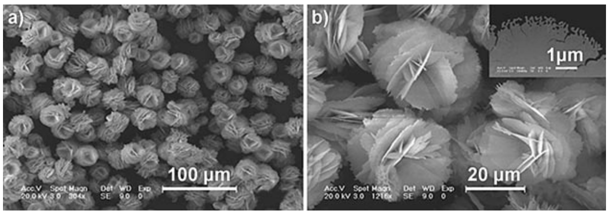

Figure 8. SEM images of sample 4 after postcalcination at 1000 °C for 4 h.

Mechanism for the $LuBO_3$:Eu^{3+} 3D structures: Enlightened by our experimental results and the previous reports,[4a, 15a,b, 21] we explain the synthesis reaction for the $LuBO_3$ phase under hydrothermal conditions simply by Equation (1).

$$Lu^{3+} + H_xBO_3^{(3-x)-} \rightarrow LuBO_3 + x\,H^+ \ (x = 0, 1, 2, 3) \qquad (1)$$

An excess of H_3BO_3 and a high pH would accelerate the reaction toward the right to form $LuBO_3$, which can be proved by the fact that increasing the amount of H_3BO_3 or the pH leads to more products being obtained under the same reaction conditions. Since lutetium exists in the form of amorphous precipitates (see Figure S5 in the Supporting Information), the dissolution of the precipitates should occur firstly, to produce Lu^{3+}. H_3BO_3 could exist in a different form because it can be ionized further under hydrothermal conditions, even though it is a weak acid. Reaction (1) above is controlled by the dissolution of the amorphous precipitates and the precipitation of $LuBO_3$ (dissolution/precipitation), which is a common mechanism in hydrothermal synthesis. At different pH values, two different phases of $LuBO_3$ were obtained (Figure 1). Although the exact mechanism of formation for this is unknown at present, the same phenomena can be found in many other reports.[18, 22]

To understand the process of formation of the $LuBO_3$:Eu^{3+}, we carried out time-dependent shape evolution experiments at pH 7 during which samples were collected after different periods of hydrothermal treatment. At an early stage (4 h) circular nanoflakes, diameter about 2.5 µm, and some tiny nanoflakes are first formed from the solution (Figure 9a). The sample collected 6 h later (Figure 9b) showed approximately 3.6 µm of primary microflowers consisting of multilayer nanoflakes. As the reaction proceeded (Figure 9c), the 3D nanostructure grew gradually (9 µm) and normal flower-like morphology developed. It is evident that flower-like crystals form in the flake aggregates (Figure 9c). Eventually, after further growth, the sample was composed entirely of fully 3D flower-like nanostructures (16 µm; Figure 9d). The whole evolution process is illustrated in Figure 10. In this formation process, the reaction time was the most important controlling factor. Such a process is consistent with previous reports of a so-called two-stage growth process, which involves a fast nucleation of amorphous primary particles followed by a slow aggregation and crystallization of primary particles.[23] The bigger particles grew at the cost of the smaller ones, because the solubility of the larger and smaller particles differs according to the Gibbs–Thomson law.[24] In the present experiment, the dissolution of the amorphous precipitates should occur first; these are then precipitated to become the nuclei and to grow rapidly

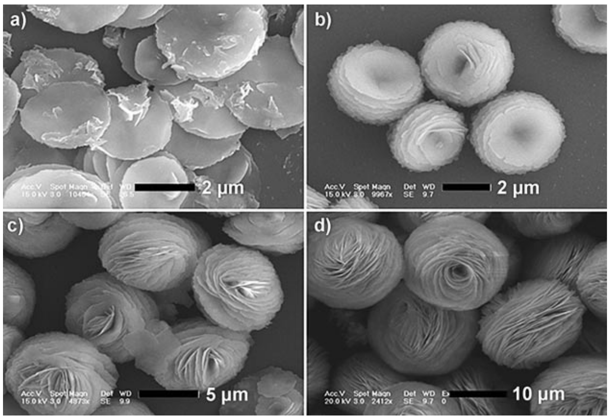

Figure 9. SEM images of the products at 200 °C obtained at different times at pH 7: a) 4 h; b) 6 h; c) 9 h; d) 24 h.

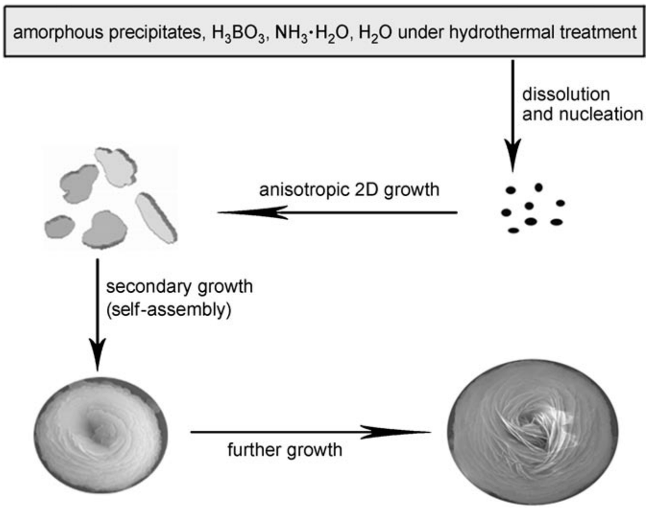

Figure 10. Illustration of the morphological evolution of the $LuBO_3:Eu^{3+}$ 3D structures.

into nanoflakes owing to the natural growth habit of rare earth orthoborates, which form a flake-like morphology during the growth process.[4a,10,15b] In the following secondary growth stage, other tiny nanoflakes extend at an angle to the plane of the first flake from the center to form primary microflowers at the expense of the amorphous precipitates and/or small crystals. The primary microflowers continue to grow in a homocentric layer-by-layer growth style,[25] and hierarchical flower-like structures are formed to reduce the surface energy. The petal surfaces in the flower-like structure are very smooth, probably owing to Ostwald ripening.[23a] The boundaries of these flowers are composed of the thin edges of many flakes. The point contact area between adjacent flowers is therefore small. This minimizes the interaction between these flowers, so that they do not agglomerate, an advantage when suspensions are used for fabricating devices where coating uniformity is important. The mechanism for the formation of the final structure morphology by interaction between primary particles remains a mystery to materials chemists,[23b] although many kinds of flower-like 3D structures have been reported.[6b,23c,25,26] Several factors, including crystal-face attraction, electrostatic and dipolar fields associated with the aggregate, van der Waals forces, hydrophobic interactions, and hydrogen bonds, may have various effects on the self-assembly.[23c,27]

Photoluminescence properties: Under short-wavelength UV light excitation, calcite-type $LuBO_3:Eu^{3+}$ (sample 1) and vaterite-type $LuBO_3:Eu^{3+}$ (sample 4) exhibit strong orange and red emission, respectively. Their excitation spectra (see Figure S6 in the Supporting Information) both consist of a broad band from $\lambda = 200$ to 300 nm owing to the charge-transfer band (CTB) between O^{2-} and Eu^{3+}. In the longer-wavelength region, the f–f transition lines of Eu^{3+} can be observed with very weak intensity compared with the Eu^{3+}–O^{2-} CTB. Their photoluminescence (PL) emission spectra from $\lambda = 500$ to 700 nm upon excitation into the CTB of Eu^{3+} at $\lambda = 254$ nm are shown in Figures 11a,b, respectively. The emission spectrum of calcite-type $LuBO_3:Eu^{3+}$ contains only two lines at $\lambda = 589$ and 594 nm (Figure 11a), which can be attributed to the $^5D_0 \rightarrow {}^7F_1$ magnetic dipole (m.d.) transition. The absence of the electric dipole (e.d.) transition (that

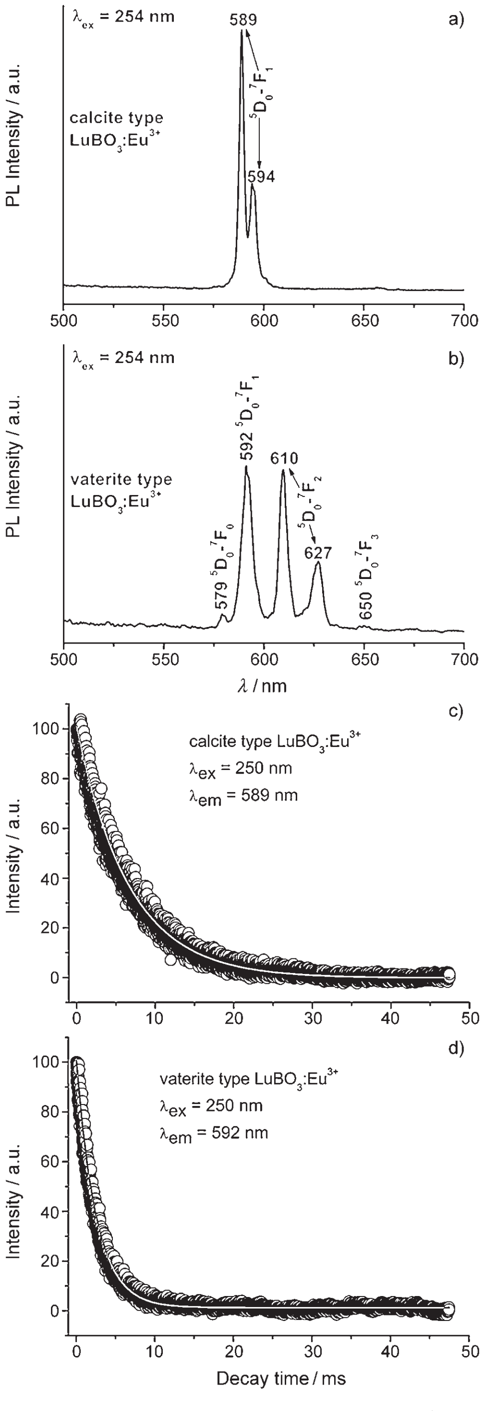

Figure 11. Emission spectra of a) calcite-type $LuBO_3:Eu^{3+}$ of sample 1 and b) vaterite-type $LuBO_3:Eu^{3+}$ of sample 4 under $\lambda = 254$ nm irradiation. Decay curves for the $^5D_0 \rightarrow {}^7F_1$ emission of Eu^{3+} in c) calcite-type $LuBO_3$ and d) vaterite-type $LuBO_3$. Circles represent experimental data; the solid line fits results to $I(t) = I_0\exp(-t/\tau)$, where c) $\tau = 6.59(\pm 0.1)$ ms; d) $\tau = 2.53(\pm 0.4)$ ms.

is, the $^5D_0 \rightarrow {}^7F_{0,2,4}$ transitions) is in excellent agreement with S_6 symmetry of the Lu site with inversion symmetry.[13b,16a] For vaterite-type $LuBO_3$:Eu^{3+}, the emission spectrum is composed of $^5D_0 \rightarrow {}^7F_J$ ($J = 0$, 1, 2, 3) transition lines of Eu^{3+} owing to a deviation from the ideal S_6 local symmetry (Figure 11b).[13b,16a] All emission peaks at $\lambda = 579$ ($^5D_0 \rightarrow {}^7F_0$), 592 ($^5D_0 \rightarrow {}^7F_1$), 610, 627 ($^5D_0 \rightarrow {}^7F_2$) and 650 nm ($^5D_0 \rightarrow {}^7F_3$) have been assigned in Figure 11b. The relative intensity of each peak in this emission spectrum is quite different from that of the solid reaction-derived sample (SR) (Figure 12), which will be discussed in more detail below.

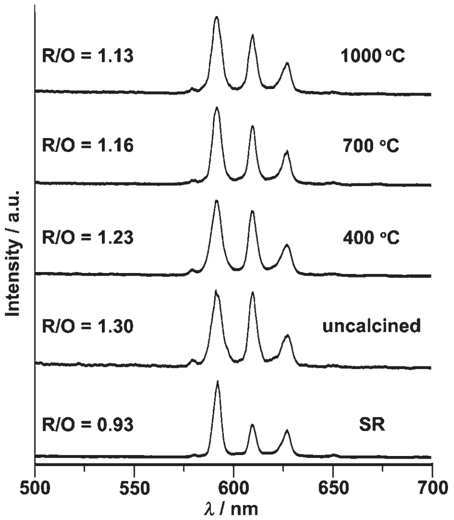

Figure 12. Normalized emission spectra of SR and sample 4 with different postcalcination temperatures under $\lambda = 254$ nm UV excitation. R/O = integrated intensity of $^5D_0 \rightarrow {}^7F_2$/integrated intensity of $^5D_0 \rightarrow {}^7F_1$.

The decay curves for the luminescence of Eu^{3+} in calcite-type $LuBO_3$ (monitored by $^5D_0 \rightarrow {}^7F_1$, $\lambda = 589$ nm) and vaterite-type $LuBO_3$ (monitored by $^5D_0 \rightarrow {}^7F_1$, $\lambda = 592$ nm) can be fitted well into a single exponential function as $I = I_0 \exp(-t/\tau)$ respectively (Figures 11c,d), in which I_0 is the initial emission intensity at $t = 0$, and τ is the 1/e lifetime of the emission center. The lifetimes for the $^5D_0$ lowest excited state of Eu^{3+} have been determined as 6.59 and 2.53 ms for calcite-type $LuBO_3$:Eu^{3+} (sample 1) and vaterite-type $LuBO_3$:Eu^{3+} (sample 4) respectively, basically agreeing with the reported values (3.10 ms) for other Eu^{3+}-doped $LuBO_3$ samples.[28]

All the normalized emission spectra of SR and sample 4 with different postcalcination temperatures under $\lambda = 254$ nm UV excitation (Figure 12) consist of sharp peaks centered at the same wavelengths of Eu^{3+}: $\lambda = 579$ ($^5D_0 \rightarrow {}^7F_0$), 592 ($^5D_0 \rightarrow {}^7F_1$), 610, 627 ($^5D_0 \rightarrow {}^7F_2$), and 650 nm ($^5D_0 \rightarrow {}^7F_3$). The $\lambda = 592$ nm emission corresponds to the orange color (O), while the $\lambda = 610$ and 627 nm emissions correspond to the red color (R).[29] Although the main peak positions in the emission spectra of all the samples are identical, the intensity patterns differ to some extent. The magnetic dipole transition $^5D_0 \rightarrow {}^7F_1$ is clearly the most prominent group in the emission spectrum of SR and the electric dipole transition $^5D_0 \rightarrow {}^7F_2$ is the primary group in the emission spectrum of sample 4; the R/O value of sample 4 (1.30) is much higher than that of SR (0.93), which means that an improved chromaticity (increased by 40 %; that is, a chromatically redder fluorescence)[30] can be obtained in these flower-like assemblies. This can be seen easily from the CIE chromaticity diagram, which shows the emission colors (see Figure S7 in the Supporting Information). This improvement is especially important for a red phosphor-like vaterite-type $LuBO_3$:Eu^{3+}, whose application has always been restricted by its relatively poor chromaticity. We attribute the improvement to the distinct microstructure of the assembly, which maintains the characteristics of the nanoflake building blocks. These nanoflakes possess especially large surface areas and high surface energies, which would not only provide a driving force for the self-assembly, but also result in a high degree of disorder near the surface and corresponding lower symmetry of crystal field around Eu^{3+} ions than in the bulk materials.[4a,10,15d] As predicted by Judd–Ofelt theory,[31] a lower symmetry of the crystal field will result in a higher R/O value. Based on this assumption, the improved chromaticity of the assembly is indeed correlated with the microstructure and crystallinity, but not the assembled particle size. By changing its degree of crystallization by means of controlled postcalcination, we may effectively adjust its luminescent properties while maintaining the assembled particle size and microstructure. With an increase in the postcalcination temperature, the emission spectrum of sample 4 experiences interesting changes (Figure 12). The PL emission intensity increases with the increase in postcalcination temperatures due to improved crystallinity (see Figure S8 in the Supporting Information). Figure 12 clearly shows the temperature-dependent characteristics of the R/O value. For the uncalcined sample, and those calcined at 400, 700, and 1000 °C, R/O was 1.30, 1.23, 1.16, and 1.13, respectively, indicating that a lower temperature (sample 4, uncalcined) was favorable to achieving superior chromaticity. A higher postcalcination temperature does not change the microstructure of the assembly with the characteristics of the building-block nanoflakes (Figure 8) which favors a higher R/O value as in the aforementioned analysis, but will lead to better crystallinity, which would cause a lower level of disorder,[32] further lowering R/O.[4a,15d] In addition, postcalcination has changed the relative numbers of the two types of Eu^{3+} local sites in the vaterite phase, which have different degrees of distortion and may induce different R/O values. From a technical point of view, 1000 °C may be the proper postcalcination temperature (much higher than the 700 °C for YBO_3:Eu^{3+} in ref. [4a]), because then the R/O value is more reasonable; higher than that of SR, with an improved chromaticity (increased by 22 %), although lower than that of sample 4 (uncalcined); moreover, the PL intensity reaches 73 % of that of SR (see Figure S8 in the Supporting Information).

Cathodoluminescence properties: Under low-voltage electron beam excitation, the as-prepared calcite-type

$LuBO_3$:Eu^{3+} and vaterite-type $LuBO_3$:Eu^{3+} particles exhibit strong orange and red emission respectively. The typical cathodoluminescence emission spectra of calcite-type $LuBO_3$:Eu^{3+} (sample 1) and vaterite-type $LuBO_3$:Eu^{3+} (sample 4 postcalcined at 1000 °C) phosphors under electron beam excitation (accelerating voltage = 2 kV; filament current = 96 mA) (Figures 13a,b, respectively) are similar to the corresponding PL emission spectra shown in Figures 11 a,b. The cathodoluminescence (CL) emission intensities for calcite-type $LuBO_3$:Eu^{3+} and vaterite-type $LuBO_3$:Eu^{3+} phosphors have been investigated as a function of the accelerating voltage and the filament current (Figures 13 c,d, respectively). When the filament current is fixed at 92 mA, the CL intensity increases with rising accelerating voltage from 1 to 3 kV (Figure 13 c). Similarly, under a 2 kV electron beam excitation, the CL intensity also increases with increasing filament current from 93 to 106 mA (Figure 13 d). For cathodoluminescence, the Eu^{3+} ions are excited by the plasma produced by the incident electrons. The electron penetration depth can be estimated from Equation (2), where $n = 1.2/(1-0.29\log_{10}Z)$, A is the atomic or molecular weight of the material, ρ is the bulk density, Z is the atomic number or the number of electrons per molecule in the case of compounds, and E is the accelerating voltage (kV).[33]

$$L[\text{Å}] = 250(A/\rho)(E/Z^{1/2})^n \qquad (2)$$

For $LuBO_3$:Eu^{3+}, the calculated electron penetration depths at 3 kV are about 27.5 nm for the calcite type and 26.2 nm for the vaterite type. With an increase in accelerating voltage, more plasma will be produced by the incident electrons, resulting in more Eu^{3+} being excited and higher CL intensity. The increase in electron energy is attributed to deeper penetration of electrons into the phosphor body, governed by Equation (2). This deeper penetration results in an increase in electron–solid interaction volume in which excitation of Eu^{3+} ions is responsible for the light emission. Therefore, an increase in interaction volume (which effectively determines the generation of light inside the phosphor) with an increase in electron energy brings about an increase in the CL brightness of $LuBO_3$:Eu^{3+} particles.[34] Due to their strong low-voltage CL intensity and improved chromaticity, calcite-type $LuBO_3$:Eu^{3+} and vaterite-type $LuBO_3$:Eu^{3+} phosphors may find possible applications in field emission display devices.

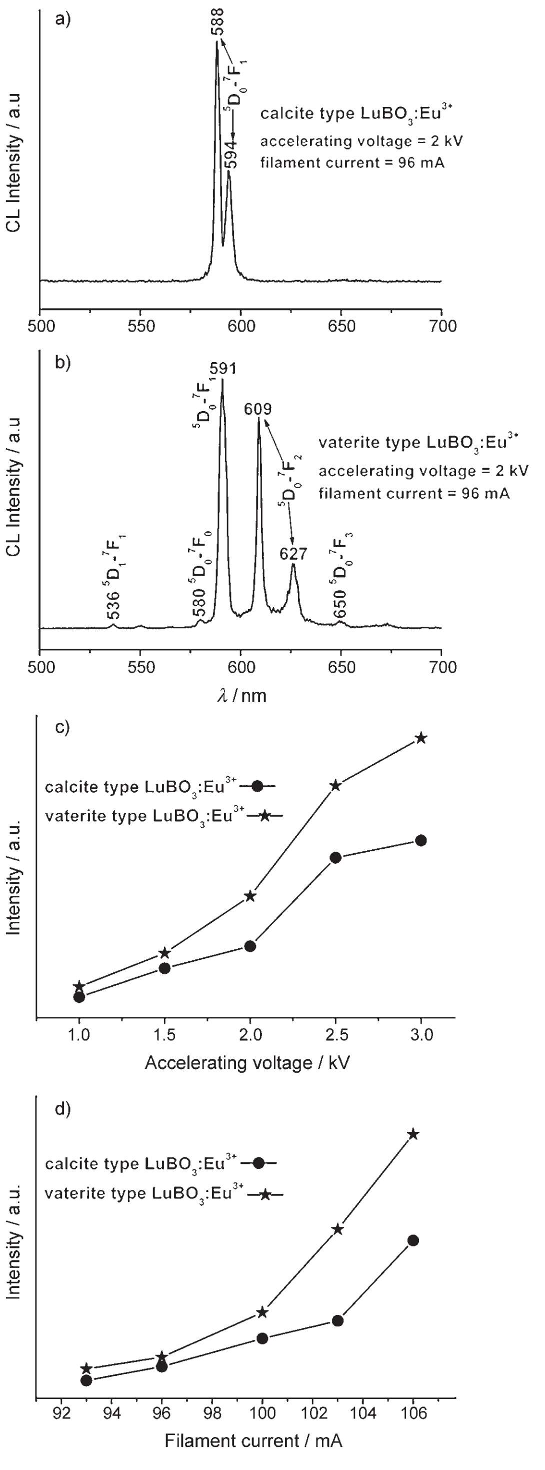

Figure 13. Typical cathodoluminescence spectra of a) calcite-type $LuBO_3$:Eu^{3+} of sample 1; b) vaterite-type $LuBO_3$:Eu^{3+} of sample 4 postcalcined at 1000 °C. The cathodoluminescence intensities of calcite-type $LuBO_3$:Eu^{3+} and vaterite-type $LuBO_3$:Eu^{3+} as a function of c) accelerating voltage; d) filament current.

Conclusion

We have demonstrated that a simple, mild hydrothermal method for the selective synthesis of novel 3D superstructures of rhombohedral-calcite and hexagonal-vaterite types of $LuBO_3$:Eu^{3+} microparticles. This simple synthetic method, which does not use any surfactant or template, may be extended to the synthesis of other materials with novel morphologies. The morphology, microstructure, crystal structure, chemical composition, and optical properties were characterized by XRD, SEM, EDX, TEM, high-resolution transmission electron microscopy (HRTEM), SAED, PL, CL, and kinetic decays. The significance of our work does not lie in the beautiful morphology of the microcrystals alone. We examined the phase formation, shape evolution, and microstructures of $LuBO_3:Eu^{3+}$ in more detail than in the previous studies of $LnBO_3$ and we found them to be strongly dependent on the reaction conditions such as the pH, temperature, concentration, solvent, and reaction time. The reaction mechanism has been considered as a dissolution/precipitation process; it has been proposed that the self-assembly evolves in a homocentric layer-by-layer growth style. Under ultraviolet excitation and low-voltage electron beam excitation, calcite-type $LuBO_3:Eu^{3+}$ particles show a strong orange emission corresponding to the $^5D_0 \rightarrow {}^7F_1$ transition of Eu^{3+}, whereas vaterite-type $LuBO_3:Eu^{3+}$ particles exhibit a strong red emission with a much higher R/O value (that is, chromatically redder fluorescence than that of crystals grown from a direct solid-state reaction) which has potential applications in fluorescent lamps and field emission displays. These 3D architectures of rhombohedral-calcite and hexagonal-vaterite types of $LuBO_3:Eu^{3+}$ microparticles with unique shapes and structural characteristics may also find applications as catalysts and in other fields.

Table 1. Experimental conditions for synthesis by hydrothermal treatment for 24 h and the corresponding phase and morphologies.

Sample	Wt. of $LuCl_3$/ $EuCl_3$ mixture [g]	Wt. of H_3BO_3 [g]	Vol. of H_2O [mL]	Vol. of DEG[a] [mL]	pH	T [°C]	Phase	Morphology
1	0.7323	0.2473	40	–	4	200	calcite form	wheel
2	0.7323	0.2473	40	–	5.5	200	calcite form + vaterite form	wheel + flower
3	0.7323	0.2473	40	–	7	200	vaterite form	flower
4	0.7323	0.2473	40	–	8	200	vaterite form	flower
5	0.7323	0.2473	40	–	8	160	vaterite form	flower
6	0.7323	0.2473	40	–	8	240	vaterite form	imperfect flower + sheet
7	0.7323	0.1856	40	–	8	200	vaterite form	sphere
8	0.7323	0.2473	20	20	8	200	vaterite form	doughnut

[a] DEG: diethylene glycol.

Experimental Section

Materials: The initial chemicals in this work, Lu_2O_3 and Eu_2O_3 (both with purity of 99.99 %; Shanghai Yuelong Non-Ferrous Metals Ltd., P.R. China), HCl, H_3BO_3, $NH_3{\cdot}H_2O$, diethylene glycol (DEG) and ethanol (all with AR purity; Beijing Fine Chemical Company, P.R. China), were used without further purification.

Preparation of samples: Firstly, Lu_2O_3 (14.9640 g) and Eu_2O_3 (0.8440 g) (molar ratio Lu/Eu = 94:6) were dissolved in dilute HCl solution (30 mL, 1:1 v/v), forming a colorless solution of $LuCl_3$ and $EuCl_3$. After evaporation followed by drying at 100 °C for 60 h in the ambient atmosphere, a mixed powder of $LuCl_3$ and $EuCl_3$ (29.2920 g) was obtained. In a typical synthesis, a mixture of $LuCl_3$ and $EuCl_3$ (0.7323 g) with H_3BO_3 (0.2473 g, 100 % excess) was dissolved in distilled water (40 mL) to form a clear aqueous solution. The solution was stirred for another 30 min. Then $NH_3{\cdot}H_2O$ (25 % wt.%, AR) was introduced dropwise to the vigorously stirred solution to pH 4. After additional agitation for 40 min, the as-obtained white colloidal precipitate was transferred to a 50 mL autoclave, sealed, and heated at 200 °C for 24 h, then cooled naturally to room temperature and denoted sample 1. The products were collected by filtration, washed with ethanol and distilled water several times, and dried in the atmosphere at 100 °C for 6 h. The detailed experimental parameters for the synthesis of some typical samples are listed in Table 1. For comparison, the bulk $LuBO_3:Eu^{3+}$ was obtained by a direct solid-state reaction using stoichiometric amounts of Lu_2O_3, Eu_2O_3 (molar ratio Lu/Eu = 94:6) and H_3BO_3 (50 % excess) at 1400 °C for 6 h in air. This sample was denoted as SR.

Characterization: The phase purity and crystallinity of the samples were examined by means of powder XRD performed on a Rigaku-Dmax 2500 diffractometer with CuK_α radiation ($\lambda = 0.15405$ nm). The morphology and structure of the samples were inspected by using a field emission scanning electron microscope equipped with an EDX spectrometer (FE-SEM, XL 30; Philips) and a transmission electron microscope. Low-resolution TEM images and SAED patterns were obtained by using a JEOL 2010 transmission electron microscope operating at 150 kV. HRTEM images were obtained by using an FEI Tecnai G2 S-Twin microscope with a field emission gun operating at 200 kV. Images were acquired digitally by means of a Gatan multiple CCD camera. PL excitation and emission spectra were recorded by means of a Hitachi F-4500 spectrophotometer equipped with a 150 W xenon lamp as the excitation source at room temperature. The CL measurements were carried out in an ultra-high-vacuum chamber ($<10^{-8}$ Torr), where the samples were excited by an electron beam at a range of 1–5 kV with different filament currents, and the spectra were recorded by using an F-4500 spectrophotometer. The luminescence decay curves were obtained from a Lecroy Wave Runner 6100 Digital Oscilloscope (1 GHz) by using a tunable laser (pulse width = 4 ns, gate = 50 ns) as the excitation (Continuum Sunlite OPO). All the measurements were performed at room temperature (RT).

Acknowledgements

This project is supported financially by the "Bairen Jihua" Foundation of the Chinese Academy of Sciences, the Ministry of Science and Technology of the People's Republic of China (2003CB314707, 2007CB935502), and the National Natural Science Foundation of China (50572103, and 20431030, 00610227). We express our thanks to Prof. Yongfeng Men for help with experiments.

---

[1] a) A. P. Alivisatas, *Science* **1996**, *271*, 933–937; b) Y. N. Xia, P. D. Yang, Y. G. Sun, Y. Y. Wu, B. Mayers, B. Gates, Y. D. Yin, F. Kim, Y. Q. Yan, *Adv. Mater.* **2003**, *15*, 353–398; c) C. Burda, X. Chen, R. Narayanan, M. A. El-Sayed, *Chem. Rev.* **2005**, *105*, 1025–1102; d) J. Zhang, X. Li, X. Sun, Y. Li, *J. Phys. Chem. B* **2005**, *109*, 12544–12548.

[2] H. Dong, X. J. Li, Q. Peng, X. Wang, J. P. Chen, Y. D. Li, *Angew. Chem.* **2005**, *117*, 2842–2845; *Angew. Chem. Int. Ed.* **2005**, *44*, 2782–2785.

[3] S. Sun, S. Weiss, A. P. Alivisatos, *Science* **1998**, *281*, 2013–2016.

[4] a) X. C. Jiang, L. D. Sun, C. H. Yan, *J. Phys. Chem. B* **2004**, *108*, 3387–3390; b) Z. G. Wei, L. D. Sun, C. S. Liao, X. C. Jiang, C. H. Yan, *J. Mater. Chem.* **2002**, *12*, 3665–3670.

[5] G. M. Whitesides, M. Boncheva, *Proc. Natl. Acad. Sci. USA* **2002**, *99*, 4769–4774.

[6] a) A. K. Boal, F. Ilhan, J. E. DeRouchey, T. Thurn-Albrecht, T. P. Russell, V. M. Rotello, *Nature* **2000**, *404*, 746–748; b) N. Zhang, W. B. Bu, Y. P. Xu, D. Y. Jiang, J. L. Shi, *J. Phys. Chem. C* **2007**, *111*,

5014–5019; c) G. Z. Wang, R. Sæterli, P. M. Rørvik, R. Holmestad, T. Grande, M. A. Einarsrud, *Chem. Mater.* **2007**, *19*, 2213–2221.

[7] J. K. Yuan, K. Laubernds, Q. H. Zhang, S. L. Suib, *J. Am. Chem. Soc.* **2003**, *125*, 4966–4967.

[8] a) M. Ren, J. H. Lin, Y. Dong, L. Q. Yong, M. Z. Su, L. P. You, *Chem. Mater.* **1999**, *11*, 1576–1580; b) Z. Wei, L. Sun, C. Liao, J. Yin, X. Jiang, C. Yan, S. Lü, *J. Phys. Chem. B* **2002**, *106*, 10610–10617; c) G. Bertrand-Chadeyron, R. Mahiou, M. El-Ghozzi, A. Arbus, D. Zambon, J. C. Cousseins, *J. Lumin.* **1997**, *72–74*, 564–566; d) L. Lou, D. Boyer, G. Chadeyron, E. Bernstein, R. Mahiou, J. Mugnier, *Opt. Mater.* **2000**, *15*, 1–6; e) D. Boyer, G. Bertrand, R. Mahiou, *J. Lumin.* **2003**, *104*, 229–237.

[9] a) Z. H. Li, J. H. Zeng, C. Chen, Y. D. Li, *J. Cryst. Growth* **2006**, *286*, 487–493; b) K. N. Kim, H. K. Jung, H. D. Park, *J. Mater. Res.* **2002**, *17*, 907–910; c) G. Bertrand-Chadeyron, M. El-Ghozzi, D. Boyer, R. Mahiou, J. C. Cousseins, *J. Alloys Compd.* **2001**, *317–318*, 183–185; d) D. Boyer, G. Bertrand-Chadeyron, R. Mahiou, C. Caperaa, J. C. Cousseins, *J. Mater. Chem.* **1999**, *9*, 211–214.

[10] J. Zhang, J. Lin, *J. Cryst. Growth* **2004**, *271*, 207–215.

[11] a) L. Zhang, C. Pedrini, C. Madej, C. Dujardin, J. C. Gâcon, B. Moine, I. Kamenskikh, A. Belsky, D. A. Shaw, M. A. MacDonald, P. Mesnard, C. Fouassier, J. C. Van't Spijker, C. W. E. Van Eijk, *Radiat. Eff. Defects Solids* **1999**, *150*, 439–444; b) M. Balcerzyk, Z. Gontarz, M. Moszynski, M. Kapusta, *J. Lumin.* **2000**, *87–89*, 963–966.

[12] G. Chadeyron, M. El-Ghozzi, R. Mahiou, A. Arbus, C. Cousseins, *J. Solid State Chem.* **1997**, *128*, 261–266.

[13] a) C. Mansuy, J. M. Nedelec, C. Dujardin, R. Mahiou, *Opt. Mater.* **2007**, *29*, 697–702; b) D. Boyer, G. Bertrand-Chadeyron, R. Mahiou, L. Lou, A. Brioude, J. Mugnier, *Opt. Mater.* **2001**, *16*, 21–27.

[14] a) C. Serre, N. Stock, T. Bein, *Inorg. Chem.* **2004**, *43*, 3159–3163; b) X. Wang, Y. D. Li, *Angew. Chem.* **2003**, *115*, 3621–3624; *Angew. Chem. Int. Ed.* **2003**, *42*, 3497–3500; c) X. Wang, X. M. Sun, D. P. Yu, B. S. Zhou, Y. D. Li, *Adv. Mater.* **2003**, *15*, 1442–1445; d) C. J. Jia, L. D. Sun, L. P. You, X. C. Jiang, F. Luo, Y. C. Pang, C. H. Yan, *J. Phys. Chem. B* **2005**, *109*, 3284–3290; e) J. Yang, C. K. Lin, Z. L. Wang, J. Lin, *Inorg. Chem.* **2006**, *45*, 8973–8979; f) J. Yang, Z. W. Quan, D. Y. Kong, X. M. Liu, J. Lin, *Cryst. Growth Des.* **2007**, *7*, 730–735.

[15] a) Z. H. Li, J. H. Zeng, Y. D. Li, *Small* **2007**, *3*, 438–443; b) X. C. Jiang, L. D. Sun, W. Feng, C. H. Yan, *Cryst. Growth Des.* **2004**, *4*, 517–520; c) Y. H. Wang, K. Uheda, H. Takizawa, T. Endo, *Chem. Lett.* **2001**, *3*, 206–207; d) X. C. Jiang, C. H. Yan, L. D. Sun, Z. G. Wei, C. S. Liao, *J. Solid State Chem.* **2003**, *175*, 245–251; e) J. Ma, Q. S. Wu, Y. P. Ding, Y. Chen, *Cryst. Growth Des.* **2007**, *7*, 1553–1560.

[16] a) J. Hälsö, *Inorg. Chim. Acta* **1987**, *139*, 257–259; b) E. M. Levin, R. S. Roth, J. B. Martin, *Am. Mineral.* **1961**, *46*, 1030–1055.

[17] J. Q. Hu, Y. Bando, J. H. Zhan, Y. B. Li, T. Sekiguchi, *Appl. Phys. Lett.* **2003**, *83*, 4414–4416.

[18] Y. Ding, S. H. Yu, C. Liu, Z. A. Zang, *Chem. Eur. J.* **2007**, *13*, 746–753.

[19] a) Y. W. Jun, S. M. Lee, N. J. Kang, J. Cheon, *J. Am. Chem. Soc.* **2001**, *123*, 5150–5151; b) Y. H. Kim, Y. W. Jun, B. H. Jun, S. M. Lee, J. Cheon, *J. Am. Chem. Soc.* **2002**, *124*, 13656–13657.

[20] J. Yang, X. M. Liu, C. X. Li, Z. W. Quan, D. Y. Kong, J. Lin, *J. Cryst. Growth* **2007**, *303*, 480–486.

[21] T. Kim, S. Kang, *Mater. Res. Bull.* **2005**, *40*, 1945–1954.

[22] a) X. J. Cui, S. H. Yu, L. L. Li, L. Biao, H. B. Li, M. S. Mo, X. M. Liu, *Chem. Eur. J.* **2004**, *10*, 218–223; b) Y. P. Fang, A. W. Xu, A. M. Qin, R. J. Yu, *Cryst. Growth Des.* **2005**, *5*, 1221–1225.

[23] a) Y. Cheng, Y. S. Wang, Y. H. Zheng, Y. Qin, *J. Phys. Chem. B* **2005**, *109*, 11548–11551; b) J. Park, V. Privman, E. Matijevic, *J. Phys. Chem. B* **2001**, *105*, 11630–11635; c) L. S. Zhong, J. S. Hu, H. P. Liang, A. M. Cao, W. G. Song, L. J. Wan, *Adv. Mater.* **2006**, *18*, 2426–2431.

[24] *Crystallization*, 3rd ed. (Eds.: J. W. Mullin), Butterworth-Heinemaan, Oxford, **1997**.

[25] L. X. Yang, Y. J. Zhu, L. Li, L. Zhang, H. Tong, W. W. Wang, G. F. Cheng, J. F. Zhu, *Eur. J. Inorg. Chem.* **2006**, 4787–4792.

[26] a) A. C. Chen, X. S. Peng, K. Koczkur, B. Miller, *Chem. Commun.* **2004**, 1964–1965; b) Y. P. Zhao, D. X. Ye, G. C. Wang, T. M. Lu, *Nano Lett.* **2002**, *2*, 351–354; c) X. S. Fang, C. H. Ye, L. D. Zhang, J. X. Zhang, J. W. Zhao, P. Yan, *Small* **2005**, *1*, 422–428; d) Y. B. Li, Y. Bando, D. Golberg, *Appl. Phys. Lett.* **2003**, *82*, 1962–1964.

[27] a) Y. Politi, T. Arad, E. Klein, S. Weiner, L. Addadi, *Science* **2004**, *306*, 1161–1164; b) H. Colfen, M. Antonietti, *Angew. Chem.* **2005**, *117*, 5714–5730; *Angew. Chem. Int. Ed.* **2005**, *44*, 5576–5591; c) H. Colfen, S. Mann, *Angew. Chem.* **2003**, *115*, 2452–2468; *Angew. Chem. Int. Ed.* **2003**, *42*, 2350–2365.

[28] G. Chadeyron-Bertrand, D. Boyer, C. Dujardin, C. Mansuy, R. Mahiou, *Nucl. Instrum. Methods Phys. Res. Sect. B* **2005**, *229*, 232–239.

[29] a) R. T. Wegh, H. Donker, K. D. Oskam, A. Meijerink, *Science* **1999**, *283*, 663–666; b) C. Feldmann, T. Justel, C. R. Ronda, D. U. Wiechert, *J. Lumin.* **2001**, *92*, 245–254.

[30] Z. G. Wei, L. D. Sun, C. S. Liao, C. H. Yan, *Appl. Phys. Lett.* **2002**, *80*, 1447–1449.

[31] B. R. Judd, *Phys. Rev.* **1962**, *127*, 750–761.

[32] a) Z. M. Qi, C. S. Shi, Y. G. Wei, Z. Wang, T. Liu, T. D. Hu, Z. Y. Zhao, F. L. Li, *J. Phys. Condens. Matter* **2001**, *13*, 11503–11509; b) Z. M. Qi, C. S. Shi, Z. Wang, Y. G. Wei, Y. N. Xie, T. D. Hu, F. L. Li, *Acta Phys. Sin.* **2001**, *50*, 1318–1323.

[33] C. Feldman, *Phys. Rev.* **1960**, *117*, 455–459.

[34] D. Kumar, K. G. Cho, Z. Chen, V. Craciun, P. H. Holloway, R. K. Singh, *Phys. Rev. B* **1999**, *60*, 13331–13334.

Received: December 13, 2007